Magnetic ordering of Fe and Tb in the *ab initio* determined FeRGe$_2$O$_7$ structure (R=Y, Tb)

C. Cascales,* L. Bucio,[†] E. Gutiérrez Puebla, and I. Rasines

Instituto de Ciencia de Materiales de Madrid, CSIC, Cantoblanco, 28049 Madrid, Spain

M. T. Fernández-Díaz

Institut Laue-Langevin, BP 156X, F-38042 Grenoble Cedex, France

The crystal structure of FeRGe$_2$O$_7$ (R=Y, Tb) has been solved *ab initio* from x-ray powder diffraction data. It is monoclinic, space group $P2_1/m$ (No. 11), $Z=4$, a (Å)=9.6552(4) and 9.6388(8); b (Å)=8.5197(3) and 8.4789(7), c (Å)=6.6746(3) and 6.7383(5), β (°)=100.761(2) and 100.377(4), and V(Å^3)=539.39 and 541.69, for R=Y and Tb, respectively. Precise oxygen positions were determined for the Tb compound from a room temperature neutron diffraction profile, refined by the Rietveld method to an R_f=3.99% using 58 parameters. The FeYGe$_2$O$_7$ crystal structure contains three kinds of coordination polyhedra: R^{3+} coordinated to seven oxygens at slightly different lengths forming a capped octahedron, FeO$_6$ distorted octahedra, and four types of GeO$_4$ tetrahedra. Its most interesting feature is the existence of flattened chains of RO$_7$ polyhedra linked in the c direction through pairs of FeO$_6$ octahedra with which they share edges, forming layers running parallel to the bc crystal plane. Magnetization measurements between 350 and 1.7 K show one peak at 38 K for R=Y and two maxima at 42 and 20 K for the Tb compound, which could indicate transitions to antiferromagnetically ordered states. From low-temperature neutron diffraction data on FeTbGe$_2$O$_7$, three-dimensional antiferromagnetic ordering is established, both Fe and Tb sublattices getting simultaneously ordered at T_N=42 K. The propagation vector of the magnetic structure is k=[0,0,0]. At 1.7 K the magnetic moments 3.91(7)μ_B (Fe^{3+}) and 7.98(6)μ_B (Tb^{3+}) lie ferromagnetically coupled in the ac planes, which contain TbO$_7$-FeO$_6$-TbO$_7$- chains in the c direction, forming relatively small angles with the c axis. The coupling between parallel ac planes is antiferromagnetic along the b direction. This model leads to a best fit of R_{mag}=3.02%. The thermal evolution of the magnetic moments suggests that below ~20 K the faster increase of the Tb^{3+} moments is due to the stronger Fe-Tb interactions and crystal field effects. The maximum in $\chi(T)$ at 20 K does not correspond then to any phase transition, but is caused by the exchange interaction with the ordered iron subsystem. [S0163-1829(98)00910-2]

I. INTRODUCTION

Single-centered crystals such as cubic garnets, orthorhombic aluminates, or tetragonal and monoclinic fluorides, when activated with trivalent lanthanides R^{3+} constitute the focus of laser-crystal physics. The possibility of introducing R^{3+} activators into single-centered hosts up to full substitution of all cations opens new opportunites for obtaining the so-called self-activated crystals. The spectroscopic study of series of such compounds is not only of great interest for the crystal field theory of R^{3+} ions, but also provides important information concerning numerous applied optical effects. The family of germanates MRGe$_2$O$_7$, in which M and R represent trivalent metals, Al, Ga, or Fe, and rare-earth ions, respectively, supplement the above-mentioned classes of single-centered compounds. Those with Al or Ga, R=La, Dy,[1,2] were found in the early 1980s to present a monoclinic AlNdGe$_2$O$_7$ structure type, space group $P2_1/c$. Detailed studies of absorption, luminescence, and stimulated emission were carried out for these Nd^{3+}-containing compounds.

In the iron family and depending on the size of R, the phase formation corresponds to the mentioned[1,3,4] monoclinic type for the larger R cations (La-Gd) and to another unkown and low-symmetry structure[5] for the smaller (Y and Tb-Yb) rare earths. The observed x-ray diffraction patterns for polycrystalline samples of yttrium and heavy rare earths

FeRGe$_2$O$_7$ germanates consist[5] of broad, unresolved reflections, and moreover the presence of Y$_2$Ge$_2$O$_7$ (Ref. 6) as a second phase in the case of FeYGe$_2$O$_7$ was detected. Then, since the existence of a new phase related to the optically interesting latter-mentioned family seems to be established, the precise determination of its crystal structure is the first step for a confident understanding of d-f interactions, mainly dealing with magnetic and optical properties. In fact, although two alternative models have been proposed[5] to explain the two characteristic T_{N1} and T_{N2} Néel temperatures ($T_{N2}<T_{N1}$) observed from magnetic and Mössbauer measurements on this series of iron and smaller lanthanide germanates, the absence of knowledge on the crystal structure did not allow one to ascertain its magnetic behavior.

In the present work the synthesis of pure FeRGe$_2$O$_7$, R=Y and Tb, was undertaken in order to determine their crystal structures, to investigate the nature of the anomalies denounced by the magnetic measurements, and to establish the magnetic structure of the low-temperature ordered phase of the Tb compound from neutron powder diffraction data. This paper reports the results of this study.

II. EXPERIMENT

A. Preparation of the samples

FeRGe$_2$O$_7$ (R=Y, Tb) were prepared as polycrystalline powder materials by solid state reaction from analytical

grade mixtures of Fe_3O_4, GeO_2, and Y_2O_3 or Tb_4O_7 at molar ratios Fe:Ge:R=1:2:1, although a slight defect of the R oxide under the stoichiometric required amounts was used in order to counteract the losses of GeO_2, especially as a vitrified product. Samples were ground and heated in air to 1150 °C for 5 days to 2 weeks with intermediate regrindings. Standard x-ray powder diffraction analysis indicated that final samples were well crystallized and appeared completely free of other phases.

B. X-ray structure determination

X-ray powder diffraction (XRPD) was obtained using a Siemens Kristalloflex 810 generator, Cu$K\alpha$ radiation (λ=1.540 598 Å), and a computer-controlled D-500 goniometer equipped with a graphite monochromator. The data for the *ab initio* structure determination as well as for the Rietveld refinements were collected at room temperature, over an angular range of $7°\leq2\theta\leq95°$, scanning in steps of 0.025° and a counting time of 10 s each step. Independently, d-spacing measurements were made at a scanning rate of 0.1° 2θ min^{-1}, using tungsten, a=3.165 24(4) Å, as an internal standard.

After being sure that all the reflections matched with those of the new pure $FeYGe_2O_7$ compound, that is, with no traces of any kind of possible competitive phases, the unit cell was ''autoindexed'' using the program TREOR.[7] The higher figure of merit solution was found to be a monoclinic cell, $a\approx9.63$ Å, $b\approx8.47$ Å, $c\approx6.73$ Å, and $\beta\approx100°$. The observed systematic absences suggested the existence of only one 2_1 axis along the b direction, and in consequence two possible space groups $P2_1$ and $P2_1/m$. The unit cell dimensions were refined, and after a careful optimization of the appropriate profile parameters, $363|F_{obs}|^2$ and $\sigma(|F_{obs}|^2)$ were extracted from the x-ray data using the program FULLPROF.[8]

From these $|F_{obs}|^2$ values, the structure was solved in the $P2_1/m$ space group (No. 11) by direct methods with the program SIRPOW.91.[9] After thoughtful geometric considerations, the 11 atoms of the unit cell were located through the 27 more intense peaks of the best-calculated electron-density map, which contains the 127 reflections and phases determined by the program. The same procedure was followed for the isostructural Tb compound, leading to similar results.

C. Crystal and magnetic structure refinements

Neutron powder diffraction (NPD) patterns were collected on the D1B and D2B powder diffractometers, at the Institut Laue-Langevin of Grenoble, using wavelenghts of 2.52 and 1.595 Å, respectively. About 10 g of sample contained in a cylindrical vanadium can and held in a liquid helium cryostat were employed in both experiments. The high flux and medium resolution of D1B were used to study the thermal evolution of the samples, in the temperature range 1.7–85 K. The diffraction patterns were collected every 1 K in 5 min in the angular range $15°\leq2\theta\leq85°$. The high resolution of D2B was used to obtain extensive and accurate structural data of $FeTbGe_2O_7$ at room temperature, over a large angular angle $10°\leq2\theta\leq155°$, in steps of 0.05°.

The Rietveld method was used to refine the crystal and magnetic structures. All the data, from X-ray as well as from

TABLE I. Lattice parameters and discrepancy factors for FeRGe$_2$O$_7$, R=Y, Tb, space group $P2_1/m$ (No. 11), Z=4.

	Y[a,b]	Tb[a,b]	Tb[b,c]	Tb[d,e]
Lattice parameters				
a (Å)	9.6552(4)	9.6388(8)	9.6377(3)	9.5975(7)
b (Å)	8.5197(3)	8.4789(7)	8.4794(2)	8.4345(9)
c (Å)	6.6746(3)	6.7383(5)	6.7383(2)	6.7216(8)
β (°)	100.761(2)	100.377(4)	100.381(2)	100.273(9)
V (Å^3)	539.39	541.69	541.65	535.39
Reliability factors (%)				
R_p	8.51	10.9	3.57	2.62
R_{expt}	9.81	9.95	2.42	1.29
χ^2	1.29	1.98	3.60	7.00
R_{Bragg}	6.64	8.56	5.90	3.57
R_{fcryst}	5.79	5.72	3.99	3.39
R_{fmag}				2.34

[a]From x-ray diffraction data.
[b]Room temperature.
[c]From D2B-ILL neutron diffraction data.
[d]From D1B-ILL neutron diffraction data.
[e]1.67 K.

neutron diffraction, were analyzed with the program FULLPROF.[8] A pseudo-Voigt function was chosen to generate the line shape of the diffraction peaks. For the D2B patterns the background was estimated from cubic splines interpolation between points corresponding to regions devoid of Bragg reflections. For the D1B patterns the background was fitted to a polinomial refinable function. These patterns were refined sequentially, taking as starting parameters of each pattern those resulting from the refinement of the preceding one. In all cases the shifts in the atomic parameters on the final refinement cycle were zero up to the four decimal place. The magnetic form factors for Tb^{3+} and Fe^{3+} were calculated from Ref. 10.

D. Magnetic measurements

A superconducting quantum interference device (SQUID) magnetometer (Quantum Design) operating from 350 to 1.7 K at 5000 Oe was used to perform the dc magnetic measurements. Diamagnetic corrections[11] for the magnetic susceptibilities were taken into account.

III. CRYSTAL STRUCTURE OF FeRGe$_2$O$_7$, R=Y, Tb

Table I summarizes the structural parameters for $FeYGe_2O_7$ and $FeTbGe_2O_7$, determined from x-ray and D2B collected data, at room temperature. Figure 1 shows the observed and calculated XRPD profile for $FeYGe_2O_7$, whereas Fig. 2 presents the corresponding NPD profile for $FeTbGe_2O_7$. The final refined positional and thermal parameters are given in Table II, and Table III consists of the main interatomic distances and angles for the Tb compound. XRPD patterns for both R=Y and Tb compounds are also available.[12]

The $FeYGe_2O_7$ structure type (II-FeRGe$_2$O$_7$) contains three kind of coordination polyhedra: The oxygen coordination polyhedra of Fe^{3+} are distorted octahedra joined in pairs
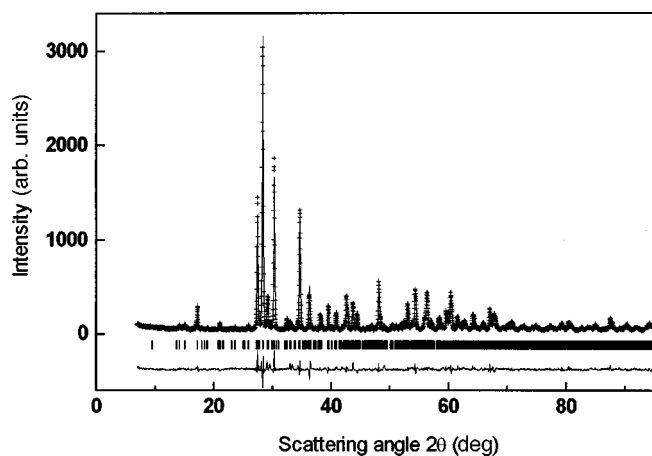
FIG. 1. Observed (crosses), calculated (solid line), and difference (at the bottom) x-ray powder diffraction profiles for FeYGe$_2$O$_7$ at room temperature. Vertical marks correspond to the position of the allowed Bragg reflections for the crystallographic structure.

by edge sharing; R^{3+} ions are coordinated to seven oxygens, the R-O distances all being of slightly different lengths; the four kind of Ge atoms exhibit the usual tetrahedral coordination, and they are associated by sharing corners forming isolated Ge(1)Ge(2)O$_7$ or Ge(3)Ge(4)O$_7$ diorthogroups, joined through O(4) or O(3), respectively. Figure 3 shows a view of the three polyhedra in the unit cell.

The results of the planarity study[13] for the Tb compound show that the shape of the TbO$_7$ polyhedron is more close to a C_{3v} capped octahedron than to a C_{2v} capped trigonal prism. In fact, four oxygen atoms O(1), O(6), O(7), and O(10) form a plane with a maximun deviation of 0.09(1) Å, the Tb atom being located very near this plane. On the contrary, because it is not possible to find any plane constituted by five oxygens, the arrangement as a pentagonal bipyramid must be discarded for the TbO$_7$ polyhedron.

RO$_7$ polyhedra are connected alternately by either a vertex or an edge into chains along the b axis, Fig. 4. For R=Tb, the closest Tb-Tb distances within these chains are 3.595(6) and 4.885(6) Å for polyhedra joined by and edge or by a corner, respectively. In the same direction only isolated pairs of associated FeO$_6$ octahedra exist, as can be seen in the same figure, and the shortest distances Fe-Fe are 3.373(4)
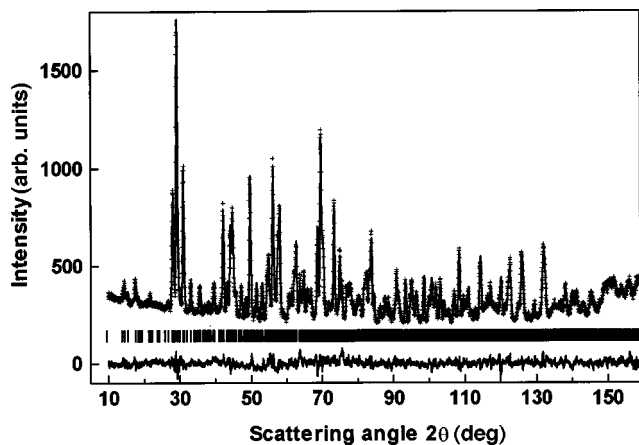
TABLE II. Final refined positional and thermal parameters from NDP (D2B) at room temperature for FeTbGe$_2$O$_7$.

	x/a	y/b	z/c	B (Å^2)
Tb	0.7543(13)	0.5880(5)	0.7565(20)	0.877(73)
Ge(1)	0.5293(12)	0.75	0.0579(14)	0.435(42)
Ge(2)	0.5513(10)	0.25	0.4978(12)	0.435(42)
Ge(3)	0.9522(11)	0.25	0.0305(13)	0.435(42)
Ge(4)	0.0251(13)	0.25	0.5373(13)	0.435(42)
Fe(1)	0.7472(12)	0.4489(3)	0.2455(17)	0.732(58)
O(1)	0.6415(11)	0.4194(11)	0.4669(17)	0.576(31)
O(2)	0.8825(17)	0.25	0.3482(22)	0.576(31)
O(3)	0.9417(12)	0.25	0.7589(18)	0.576(31)
O(4)	0.5791(11)	0.25	0.7581(18)	0.576(31)
O(5)	0.8679(10)	0.0658(11)	0.0398(16)	0.576(31)
O(6)	0.1204(18)	0.25	0.1500(24)	0.576(31)
O(7)	0.1323(12)	0.0795(11)	0.5472(17)	0.576(31)
O(8)	0.3780(18)	0.25	0.3539(24)	0.576(31)
O(9)	0.6215(18)	0.25	0.1397(23)	0.576(31)
O(10)	0.6402(13)	0.5924(12)	0.0479(17)	0.576(31)

Å inside a pair of octahedra or 5.106(4) Å between two of these groups, respectively.

Flattened chains of RO$_7$ polyhedra are linked in the c direction through pairs of FeO$_6$ octahedra with which they share edges forming layers running parallel to the bc crystal plane, as is represented in Fig. 5. Along the c axis the intermetallic distances for the Tb compound are two short Tb-Fe distances 3.393(2) and 3.514(2) Å, and those corresponding to Tb-Tb and Fe-Fe are 6.7383(16) and 6.7383(19) Å, respectively, whereas between the layers they are in the ranges 5.293(2)–6.917(2), 5.359(2)–6.889(1), and 4.808(2)–6.949(1) Å, for Tb-Tb, Fe-Fe, and Tb-Fe, respectively.

Although Ge(1)Ge(2)O$_7$ and Ge(3)Ge(4)O$_7$ diorthogroups are not connected neither in the a or b directions, they play a bridging role between parallel TbO$_7$- and FeO$_6$-containing sheets, as Fig. 5 and the insets show. In a more detailed way, in Ge(1)O$_4$, the common vertex with Ge(2)O$_4$, O(4), is also shared with TbO$_7$, and O(9) constitutes a common vertex of one FeO$_6$ pair, both polyhedra situated in the above layer, whereas the two remaining corners are partaked by RO$_7$ and FeO$_6$ in the sheet down; Ge(2)O$_4$ shares two vertexes O(1) and O(1') with common corners to TbO$_7$ and FeO$_6$ octahedra in the layer up, which is connected to the next layer through its remaining vertex O(8), shared with a RO$_7$ polyhedron; O(6) of Ge(3)O$_4$ belongs to two edge-sharing RO$_7$, in the layer above, and the two remaining vertexes are shared with common corners to RO$_7$ and FeO$_6$ of the adjacent plane. Ge(4)O$_4$ shares O(7) and O(7') with common vertexes to RO$_7$ and FeO$_6$ of one bc layer and its remaining vertex O(2) with a common corner to one double FeO$_6$ group of the sheet down. It must be noted that Ge(2)O(4) is the only of these four kind of tetrahedra having a shared edge O(1)-O(4) with another polyhedron RO$_7$.

In this II-FeRGe$_2$O$_7$ structure (R=Y, Tb-Lu), each of the oxygen atoms is coordinated to three cations, giving rise to a rather compact packing, as the cell volume per oxygen atom, Å^3 atom^{-1}, 19.26(6) and 19.35(4) for R=Y, Tb, indicates.

FIG. 2. Observed, calculated, and difference neutron diffraction (D2B, ILL) profiles of FeTbGe$_2$O$_7$ at room temperature.

TABLE III. Main interatomic distances (Å) and angles (°) in FeTbGe$_2$O$_7$.

Tb-O(1)	2.289(11)	Ge(1)-O(4)	1.760(2)
Tb-O(4)	2.970(19)	Ge(1)-O(9)	1.786(2)
Tb-O(5)	2.205(10)	Ge(1)-O(10)	1.720(16)×2
Tb-O(6)	2.194(22)	Ge(2)-O(1)	1.708(16)×2
Tb-O(7)	2.513(7)	Ge(2)-O(4)	1.739(1)
Tb-O(8)	2.251(21)	Ge(2)-O(8)	1.769(2)
Tb-O(10)	2.460(8)	Ge(3)-O(3)	1.8146(2)
Fe-O(1)	1.968(8)	Ge(3)-O(5)	1.767(16)×2
Fe-O(2)	2.167(19)	Ge(3)-O(6)	1.675(16)
Fe-O(5)	1.967(8)	Ge(4)-O(2)	1.698(2)
Fe-O(7)	1.986(13)	Ge(4)-O(3)	1.819(1)
Fe-O(9)	2.123(19)	Ge(4)-O(7)	1.771(16)×2
Fe-O(10)	1.955(14)		
O1-Tb-O(4)	57.2(4)	O(2)-Fe-O(5)	77.2(5)
O1-Tb-O(5)	130.4(9)	O(2)-Fe-O(7)	88.1(5)
O1-Tb-O(6)	139.2(6)	O(2)-Fe-O(9)	76.3(7)
O1-Tb-O(7)	64.9(3)	O(2)-Fe-O(10)	156.2(4)
O1-Tb-O(8)	85.2(4)	O(7)-Fe-O(5)	100.7(5)
O1-Tb-O(10)	123.4(4)	O(9)-Fe-O(5)	95.0(5)
O4-Tb-O(5)	82.1(6)	O(9)-Fe-O(7)	154.8(6)
O4-Tb-O(6)	163.1(1)	O(9)-Fe-O(10)	93.8(5)
O4-Tb-O(7)	116.7(5)	O(10)-Fe-O(5)	82.3(4)
O4-Tb-O(8)	111.7(4)	O(10)-Fe-O(7)	107.6(9)
O4-Tb-O(10)	79.4(4)	O(4)-Ge(1)-O(9)	91.035(2)
O6-Tb-O(5)	85.2(5)	O(4)-Ge(1)-O(10)	118.7(7)×2
O6-Tb-O(7)	79.7(4)	O(9)-Ge(1)-O(10)	113.5(7)×2
O6-Tb-O(8)	72.0(7)	O(10)-Ge(1)-O(10)	102.0(6)
O7-Tb-O(5)	122.7(4)	O(1)-Ge(2)-O(1)	114.4(6)
O8-Tb-O(5)	140.2(6)	O(1)-Ge(2)-O(4)	97.3(5)×2
O8-Tb-O(7)	85.6(5)	O(1)-Ge(2)-O(8)	112.9(8)×2
O10-Tb-O(5)	66.9(4)	O(4)-Ge(2)-O(8)	120.496(1)
O10-Tb-O(6)	85.4(5)	O(5)-Ge(3)-O(3)	95.3(5)×2
O10-Tb-O(7)	161.1(9)	O(5)-Ge(3)-O(5)	124.3(5)
O10-Tb-O(8)	78.8(4)	O(5)-Ge(3)-O(6)	113.2(9)×2
O1-Fe-O(2)	91.3(5)	O(6)-Ge(3)-O(3)	110.962(1)
O1-Fe-O(5)	168.1(9)	O(2)-Ge(4)-O(3)	101.449(2)
O1-Fe-O(7)	81.6(4)	O(2)-Ge(4)-O(7)	114.6(8)×2
O1-Fe-O(9)	79.1(5)	O(3)-Ge(4)-O(7)	108.1(6)×2
O1-Fe-O(10)	108.3(5)	O(7)-Ge(4)-O(7)	109.4(5)

These values can be compared with other values for differently packed germanates, e.g., monoclinic CuNd$_2$Ge$_2$O$_8$ (Ref. 14) and triclinic CuYb$_2$Ge$_4$O$_{12}$,[15] 20.6(5) and 20.7(2), respectively, and with those corresponding to I-FeRGe$_2$O$_7$ (R=La, Pr, Nd, Gd),[4] which range between 20.2(2) and 19.20(9) Å^3 atom^{-1}.

Although with a unique stoichiometry, both I- and II-FeRGe$_2$O$_7$ present important differences when their coordination polyhedra, especially those of the rare-earth and iron cations, are compared. If (I) presents tricapped trigonal prisms RO$_9$ and isolated trigonal bipyramids FeO$_5$, (II) contains RO$_7$ capped octahedra and isolated, edge-sharing FeO$_6$ pairs, whereas there are two and four different types of GeO$_4$ tetrahedra for (I) and (II) structures, respectively.
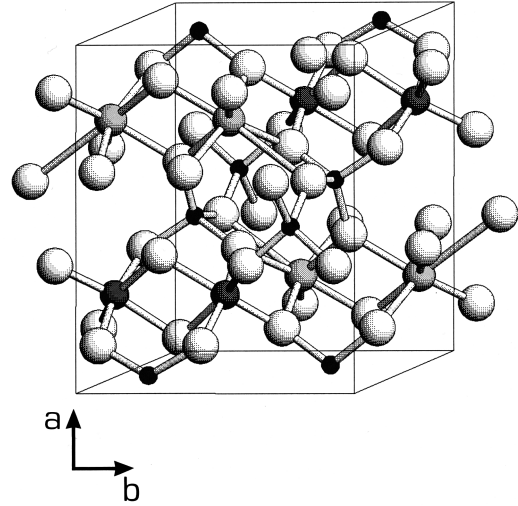
FIG. 3. View of the three kinds of polyhedra present in the unit cell of the FeYGe$_2$O$_7$ structure type. Light, medium, and dark filled spheres represent Tb, Fe, and Ge, respectively; large spheres are O atoms.

IV. MAGNETIC PROPERTIES

Figures 6 and 7 show the variation with temperature of the magnetic susceptibility χ for FeRGe$_2$O$_7$, R=Y, Tb. For the Y compound a clear maximum is observed at 38 K, which indicates a transition to an antiferromagnetically ordered state for the Fe^{3+} sublattice. At temperatures above T_N the evolution of the magnetic susceptibility presents a Curie-Weiss behavior $\chi^{-1} = 9537(20) + 98.18(9)$ T g emu^{-1}, $r = 0.9999$, with a large paramagnetic Curie temperature $\theta_C = -97.1(2)$ K and an effective magnetic moment $\mu_{eff} = 5.8(1)\mu_B$, which is very close to that of high-spin Fe^{3+} ($5.9\mu_B$).

The curve for FeTbGe$_2$O$_7$ presents a broad maximun from 43 to 31 K, also attributed to tridimensional antiferromagnetic ordering in both Fe^{3+} and Tb^{3+} sublattices. These data reveal the presence of two different anomalies in the thermal evolution of the susceptibility, at 42 and 20 K, visible in the
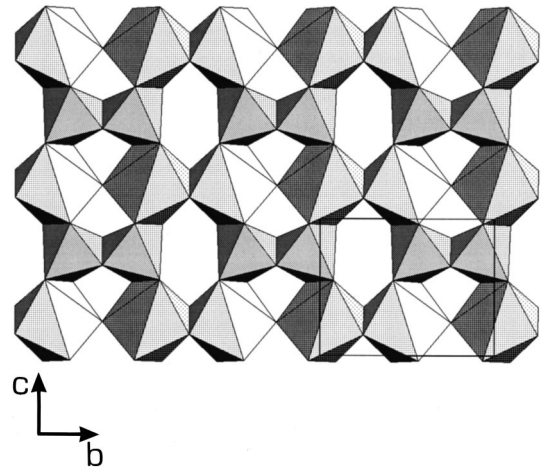
FIG. 4. Projection in the bc plane of the FeYGe$_2$O$_7$ structure, depicting the RO$_7$ chains along the b axis linked in the c direction through the pairs of FeO$_6$.
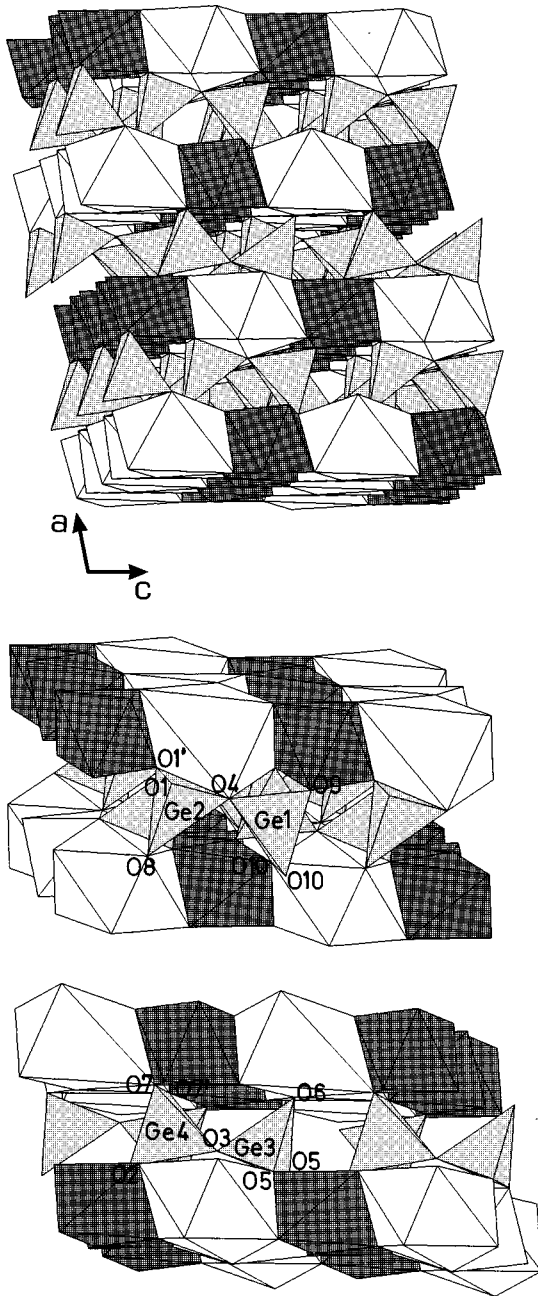
FIG. 5. Complete view of the FeYGe$_2$O$_7$ structure type showing the parallel layers resulting from the association in the bc plane of chains of RO$_7$-capped octahedra and isolated pairs of edge-sharing FeO$_6$ octahedra linked through Ge$_2$O$_7$ diorthogroups. Insets (a) and (b) display details of connectivities of Ge(1)Ge(2)O$_7$ and Ge(3)Ge(4)O$_7$, respectively.

$d(\chi T)/dT$ vs T curve. At higher temperatures the susceptibility also obeys a Curie-Weiss law $\chi^{-1} = 231(6) + 34.47(2)\, T$ g emu^{-1}, $r = 0.9999$, with $\theta_C = -6.9(2)$ K and $\mu_{\mathrm{eff}} = 10.5(1)\mu_B$.

V. MAGNETIC ORDERING IN FeTbGe$_2$O$_7$

The evolution of the NPD patterns for FeTbGe$_2$O$_7$ in a range for the 2θ scattering angle from 5° to 85° and temperatures from 1.67 to 48 K is presented in Fig. 8. A series of
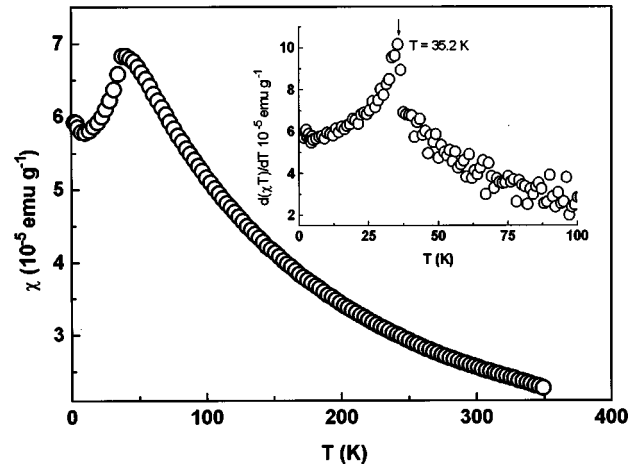
FIG. 6. Magnetic susceptibility $\chi(T)$ for FeYGe$_2$O$_7$. The inset shows the dependence of the derivative with respect to the temperature of the product χT.

extra peaks appears below 45 K, corresponding to the three-dimensional antiferromagnetic ordering of the sample. The intensities of the magnetic reflections grow regularly to reach a maximun at 1.67 K.

The temperature dependence of the lattice parameters is presented in Fig. 9, which shows that the thermal expansion in the narrow temperature range 1.67–58 K is anisotropic. Whereas b and c are almost constant, a shows a clear positive dependence on temperature with a change in the slope above ≈ 25 K.

Below 45 K all the observed Bragg peaks were indexed within a commensurate lattice with the same unit cell parameters of the crystallographic one. Reflections indexed as $0k0$, $k = 2n + 1$, an extinction condition of $P2_1/m$, were identified as ''pure magnetic'' reflections (for example, 010, the most intense reflection in Fig. 8). Initially this was an indication of the existence of some ordering of the magnetic moments perpendicular to the b axis, a supposition which can be acceptably justified by examining the expression[16] of the intensity of the nonpolarized neutron beam diffracted by a powdered sample.
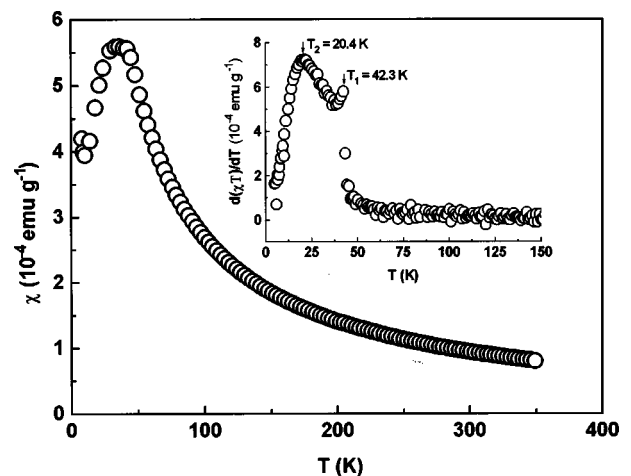
FIG. 7. Magnetic susceptibility $\chi(T)$ for FeTbGe$_2$O$_7$. In the inset, a second anomaly appears in $d(\chi T)dT$.
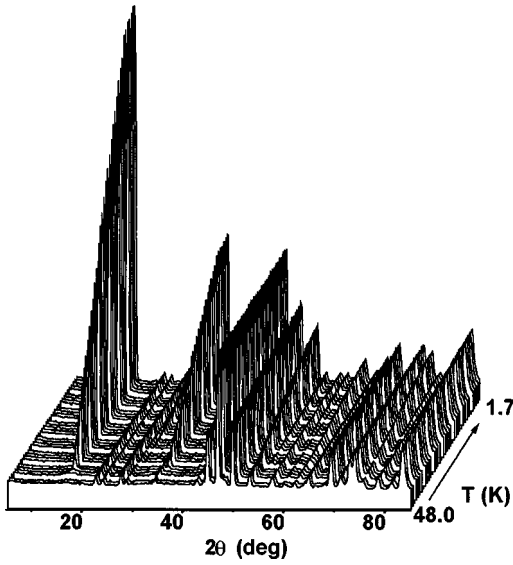
FIG. 8. Thermal evolution of the neutron diffraction patterns of FeTbGe$_2$O$_7$.

VI. GROUP THEORY ANALYSIS FOR FeTbGe$_2$O$_7$

The chemical unit cell contains four Tb and four Fe atoms. Since the lattice is primitive, the magnetic structure can be described by considering the magnetic moments of one Tb and one Fe atom, and the remaining magnetic moments can be deduced by means of the t_N Bravais translation vector, according to

$$m_{J_N} = m_{J_0} e^{-2\pi i k t_N}. \tag{1}$$

Because the magnetic and chemical unit cells are identical, this ordered magnetic structure can be described in terms of a $\mathbf{k} = [0,0,0]$ propagation vector.

Following the method described in Ref. 17, which gives the possible magnetic structures compatible with the crystal symmetry, all possible forms of ordering of the magnetic moments are determined through the base functions of the irreducible representations of the wave vector group G_k, which contains only those symmetry operations of the high-temperature space group ($T > T_N$) which keep invariant the propagation vector or transforms it into an equivalent vector. They are in our case $\{E, m_y, 2_y, i\}$, representing the identity, a mirror perpendicular to the b axis, a binary axis along b, and the inversion, respectively. Because of the axial character of the pseudovectors of the magnetic moments, a time reversal θ must be considered when the two last symmetry operations were applied.

Regarding the Tb sublattice, only one atom of Tb located at general positions $4f$ (x,y,z) generates the whole sublattice, that is, the other remaining Tb atoms, with coordinates $(x, \overline{y} + 1/2, z)$, $(\overline{x}, 1/2 + y, \overline{z})$, and $(\overline{x}, \overline{y}, \overline{z})$. The transformation properties of the components of the magnetic moment under the symmetry operations of the group G_k define a representation Γ constituted by four 3×3 matrices, the last two multiplied by the time reversal operator θ, which reverses all components of the magnetic moments, whose traces are 3, -1, -1, and 3 for the four symmetry elements. Table IV gives the characters of the irreducible representations of Γ^ν of G_k.
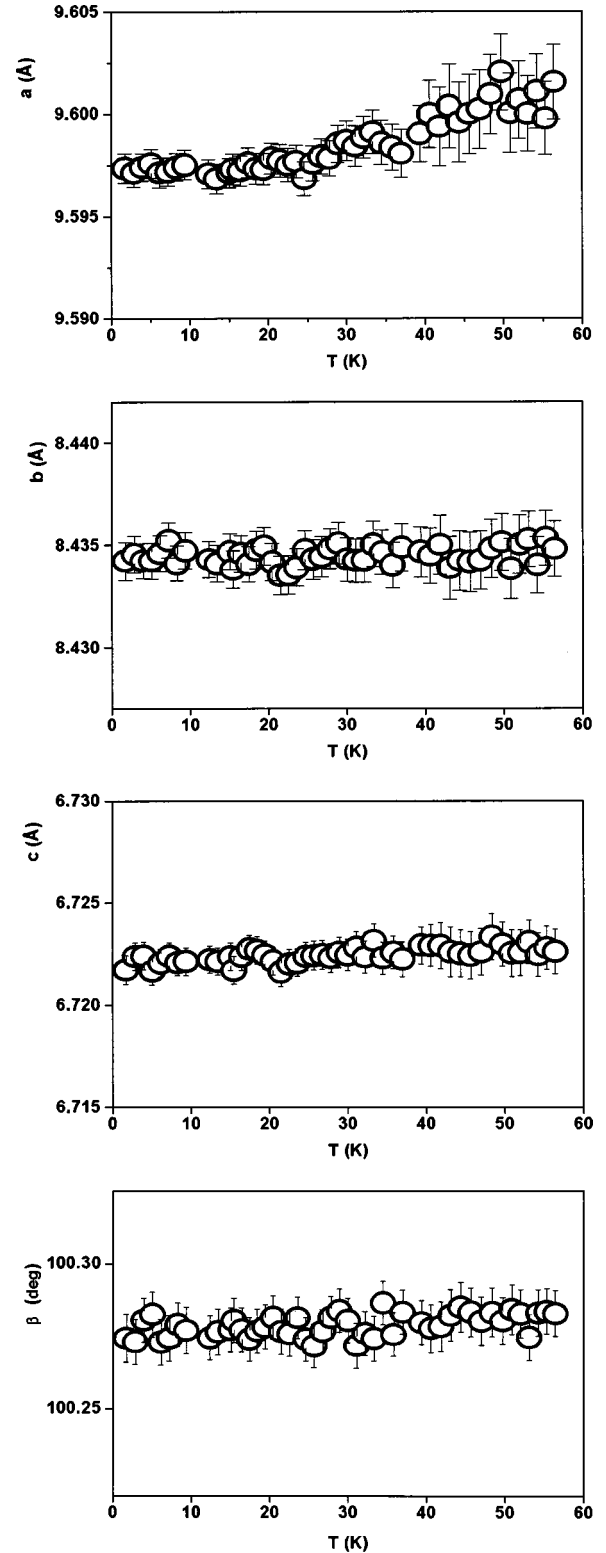
FIG. 9. Thermal variation of the a, b, c, and β lattice parameters.

In the same way, also the whole Fe sublattice results generated through one Fe atom in $4f$ positions. Table V presents the transformation rules of the magnetic moment components for both Tb and Fe. The characters of the representation Γ of Fe are 3, -1, -1, and 3 for the four symmetry elements.

Thus the irreducible representations contained in $\Gamma(\text{Tb}^{3+})$

TABLE IV. Character of the irreducible representations of $G_k(2/m)$, with $k=[0,0,0]$ of $G=P2_1/m$.

	E	m_y	$2y$	i
A_g	1	1	1	1
B_g	1	-1	-1	1
A_u	1	-1	1	-1
B_u	1	1	-1	-1

and $\Gamma(Fe^{3+})$ are, in both cases, $A_g + 2B_g$. Following Ref. 17, only vectors belonging to the same representation of both sites (Tb and Fe) may be coupled, in a first approximation. This result indicates two possibilities for the ordering of the magnetic moments of both Tb and Fe. These possibilities were analyzed by means of the basis functions obtained through the projection operator, which for an unidimensional representation is

$$\Psi_\alpha^{(\mu)} = \sum_j \chi_\mu(C_j) C_j m_\alpha, \tag{2}$$

where $\Psi_\alpha^{(\mu)}$ is the basis function, $\chi_\mu(C_j)$ the character of the irreducible representation μ corresponding to the C_j operation, and m_α is the α component of a given magnetic moment. The basis vectors for Tb^{3+} and Fe^{3+} sublattices, merely the S_α ($\alpha = x,y,z$) components of the magnetic moments, are included in Table VI. In both cases, for $\Gamma^1(A_g)$ the magnetic moments have a single component along the b axis, whereas for $\Gamma^2(B_g)$ the moment is described by the x and z components, in the ac plane.

VII. MAGNETIC SRUCTURE REFINEMENTS

The situation represented by the first A_g representation must be discarded because as previously indicated it does not correspond to the experimental data. B_g, which considers the Tb^{3+} and Fe^{3+} magnetic moments restricted to the ac plane, offers two possibilities of coupling between these atoms: the antiferromagnetic or the ferromagnetic mode, $A_x = m_{xFe} - m_{xTb}$, $A_z = m_{zFe} - m_{zTb}$, and $F_x = m_{xFe} + m_{xTb}$, $F_z = m_{zFe} + m_{zTb}$, respectively. The best fit of the experimental data at 1.67 K is obtained for the B_g representation, these data being favorably explained by the ferromagnetic coupling between the magnetic moments of Fe^{3+} and Tb^{3+} in the ac planes.

For the analysis of the low-temperature diffraction data of $FeTbGe_2O_7$, a multipattern refinement was performed. The crystal structure was refined taking as starting parameters those obtained for the data collected at room temperature. The magnetic structure was refined as an independent phase for which only magnetic atoms were defined and only mag-

TABLE V. Transformation properties of the components of the magnetic moments for Fe and Tb under the symmetry operations of G_k.

		E	m_y	2_y	i
Fe,Tb	m_x	1	-1	-1	1
	m_y	1	1	1	1
	m_z	1	-1	-1	1

TABLE VI. Basis vectors for the Fe and Tb sublattices.

	Fe			Tb		
	x	y	z	x	y	z
$\Gamma^1\ A_g$		S_y			S_y	
$\Gamma^2\ B_g$	S_x		S_z	S_x		S_z

netic scattering was calculated. The scale factors and thermal factors were constrained for both chemical and magnetic structures. Moreover, in the starting step of the analysis of the neutron diffraction data by the Rietveld method, the magnetic moments were considered as aligned along the c axis.

Tables I and VII show a summary of the refined structural parameters and magnetic moments at 1.67 K, respectively. The magnetic moments are written in the cartesian components allowed by the magnetic structure ($S_x, 0, S_z$) as well as in spherical coordinates. The Bragg discrepancy factor for the magnetic reflections was $R_{mag} = 3.02$. In Fig. 10 the observed and calculated patterns at this temperature are represented. The magnetic structure of $FeTbGe_2O_7$ consists of a ferromagnetic arrangement of the Tb^{3+} and Fe^{3+} magnetic moments along all the parallel, aligned with c-TbO_7-FeO_6-TbO_7 chains within one ac plane, whose directions form relatively small angles with the c direction, while the corresponding to adjacent up and down stacked perpendicular to b planes are antiparallel, leading then to three-dimensional (3D) antiferromagnetic coupling along the b direction. Figure 11a shows a schematic view of the magnetic structure on the ac plane containing parallel chains of edge-sharing TbO_7 and FeO_6 polyhedra along the c axis. Figure 11(b) is the projection of the magnetic structure onto bc planes.

VIII. THERMAL EVOLUTION OF THE ORDERED MAGNETIC MOMENTS OF FeTbGe₂O₇

The Fe^{3+} and Tb^{3+} magnetic moments were also refined from the neutron diffraction patterns collected on D1B as a function of the temperature. Their thermal variation is represented in Fig. 12, and it is clearly depicted that the ordering temperature is the same in both sublattices. The tridimensional magnetic order begins to develop below 42 K, the important error bars around the ordering temperature being due to the small ordered moment. The magnetic moment of Tb^{3+} increases gradually with an almost linear behavior and reaches its saturation value ($7.9\mu_B$) around 8 K. Inside this temperature range a change in the slope is detected around 20 K. The Fe^{3+} moment increases rapidly and reaches a saturation value of $3.9\mu_B$ close to 18 K.

TABLE VII. Magnetic moments for Fe^{3+} and Tb^{3+} in $FeTbGe_2O_7$ at 1.67 K, in Cartesian and spherical coordinates ($R_{mag} = 3.02$).

	S_x (μ_B)	S_z (μ_B)	M (μ_B)	θ (°)
Fe^{3+}	0.84(12)	3.97(8)	3.91(7)	12.2(6)
Tb^{3+}	3.22(11)	7.90(7)	7.98(6)	23.4(6)
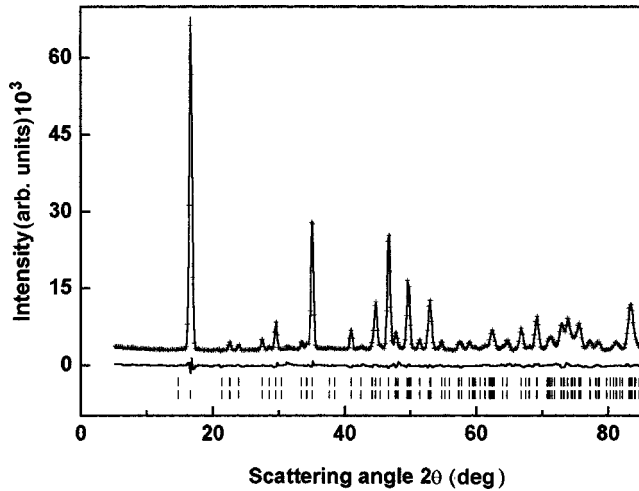
FIG. 10. Neutron diffraction pattern of FeTbGe$_2$O$_7$ (D1B, ILL) at 1.67 K. The solid line is the calculated profile, and vertical marks correspond to the position of the Bragg reflections for the crystallographic (first row) and magnetic (second row) structures. The difference curve is plotted at the bottom of the figure.

IX. DISCUSSION

In the magnetically disordered phase FeTbGe$_2$O$_7$, above the Néel temperature $T_N = 42$ K, the randomly oriented magnetic moments of Fe and Tb give rise to an incoherent contribution to the background of the neutron diffraction patterns, which disappears when the magnetic ordering is reached. This effect and the very strong intensity of the antiferromagnetic Bragg peaks are related to the high value of the magnetic moment of the Tb^{3+} ions.

Both sublattices begin to present a three-dimensional ordering at the same temperature, 42 K, and thus only one irreducible representation is favored in the transition. However, in a similar way to the behavior described[18] for R_2BaNiO$_5$ compounds, other system with magnetic interactions between $4f$ and $3d$ ions, the $d(\chi T)/dT$ vs T curve reveals the presence of two separated anomalies, at $T_1 = 42$ K and $T_2 = 20$ K, which could be attributed to the existence of two different phase transitions. Nevertheless, the analysis of the current neutron data indicates that the Néel temperature T_N coincides with T_1 and also confirms that no magnetic phase transition or spin reorientation occurs at T_2. Thus the main features of $\chi(T)$ and particularly the two separated anomalies have their origin in the Fe-Fe and Fe-Tb exchanges, as can be viewed in the thermal variation of the magnetic moments of both lattices presented in Fig. 12: Below T_N ($=T_1$) the Tb^{3+} moments become simply polarized under the local effective field from ordered Fe^{3+} moments, and the faster increase, appreciated as a subtle change in the slope, of the curve of the Tb^{3+} moments below $T_2 \sim 20$ K, is due to the stronger Fe-Tb interactions and crystal field effects on Tb^{3+} ground state manifold. This kind of explanation for the disagreement between the temperature of the broad observed maximum, supposed to be the Néel temperature, and the setting up of the magnetic ordering revealed by neutron diffraction, is sustained for rare-earth cuprates and nickelates R_2Cu$_2$O$_5$ (R=Tb-Lu; Y, Sc, In, and R_2BaMO$_5$
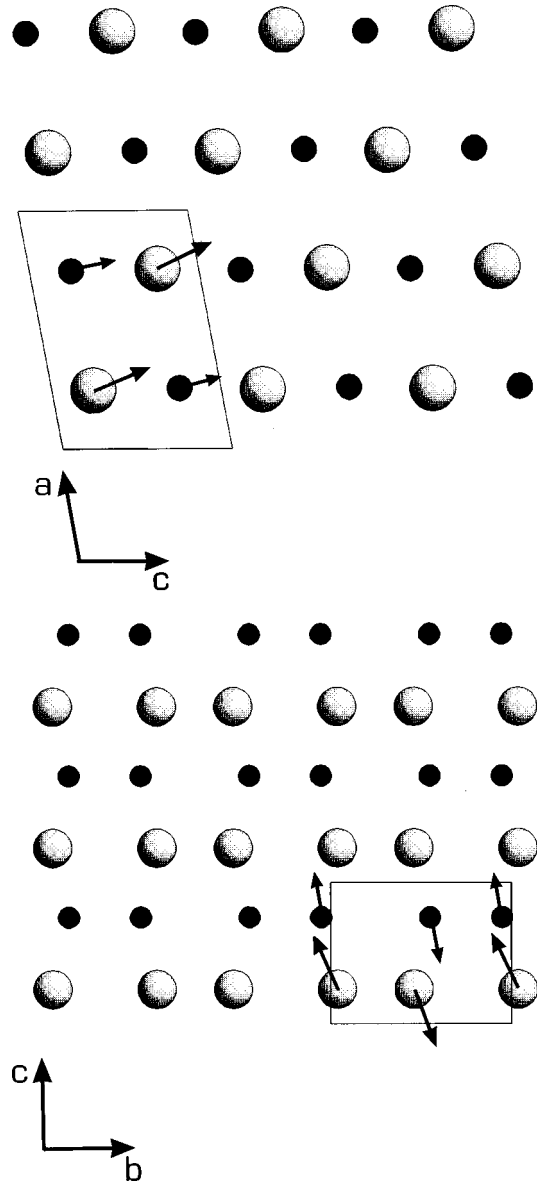
FIG. 11. Projection of the magnetic structure onto (a) ac planes and (b) bc planes. Small and large spheres representing Fe and Tb atoms, respectively.

(M=Cu, Ni),[19,20] where high-resolution spectroscopy measurements have shown that the maximum in $\chi(T)$, for Er$_2$BaNiO$_5$, for example, which was wrongly attributed to a 3D antiferromagnetic ordering,[21] does not correspond to this phase transition but it is caused by the population changes within the ground Er^{3+} Kramers doublet split by the exchange interaction with the ordered nickel subsystem.

Finally, let us consider the two alternative models[5] proposed to represent the magnetic properties of "nominal" FeRGe$_2$O$_7$, R=Y, Tb-Yb, compounds, constituted mainly by the currently described phase. The two observed characteristic temperatures $T_{N1} = 60$ K and $T_{N2} = 34$ K in the case of FeTbGe$_2$O$_7$ were assigned to the magnetic ordering of Fe^{3+} and Tb^{3+}, respectively. The first of these models, which assumes that the rare-earth and iron subsystems are not coupled, being the antiferromagnetic structures formed such that the resultant exchange interaction between them is zero, and thus the ordering in the R^{3+} sublattice caused by the
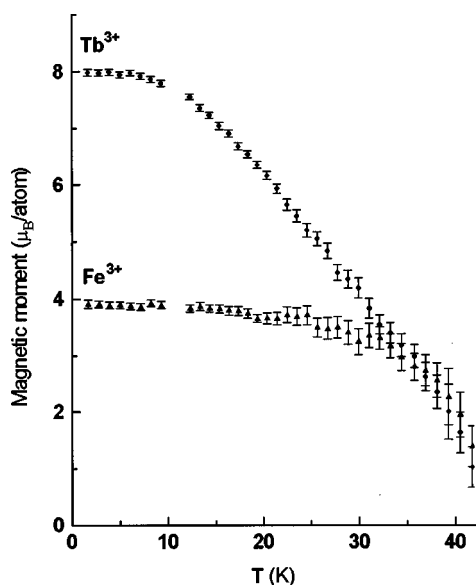
FIG. 12. Thermal evolution of the ordered magnetic moments of Fe^{3+} and Tb^{3+} in $FeTbGe_2O_7$.

intrinsic R-R exchange interaction, is not any more supported to the light of the present low-temperature neutron diffraction results. Besides the fact that the ordering of both kinds of magnetic ions occurs at the same temperature and

that no kind of magnetic order exists above 42 K, the temperatures attributed to the magnetic ordering of R^{3+}, 34 K for Tb^{3+}, are too high for the R-R exchange interaction in oxides, these temperatures being not more than a few kelvin. The other possibility supposes that for $T < T_{N1}$ the R^{3+} sublattice is in an exchange field due to the R-Fe interaction. The R-Fe exchange interaction would be weaker than that for Fe-Fe, and so, when $T_{N2} < T < T_{N1}$, the rare-earth system is weakly magnetized. When the temperature falls and the thermal energy becomes comparable with the R-Fe exchange interaction energy, the magnetic ordering in the rare-earth sublattice increases considerably and the magnetic susceptibility reaches its maximun at T_{N2}. This second model could be considered more adequate as well as the explanation for the lowest maximum of the magnetic susceptibility, understanding that the given temperatures are not the same.

ACKNOWLEDGMENTS

*Author to whom correspondence should be addressed. FAX: 34-1-372-0623. Electronic address: immcc53@fresno.csic.es.

†Present address: Departamento de Estado Sólido, Instituto de Física, UNAM, Apdo. Postal 20-364, 01000 Mexico DF, Mexico.

[1] A. A. Kaminskii, B. V. Mill, A. V. Butashin, E. L. Belokoneva, and K. Kurbanov, Phys. Status Solidi A **103**, 575 (1987).

[2] K. Jarchow, K. H. Klaska, and H. Schenk-Strauss, Z. Kristallogr. **172**, 159 (1985).

[3] B. V. Mill, S. A. Kazei, S. Y. Reiman, S. A. Tamazyan, F. D. Khamdamov, and L. Yu. Bykova, Vestn. Mosk. Univ. Fiz. Astron. **28**, 95 (1987).

[4] L. Bucio, C. Cascales, J. A. Alonso, and I. Rasines, J. Phys.: Condens. Matter **8**, 2641 (1996).

[5] Z. A. Kazei, Y. A. Kuyanov, R. Z. Levitin, A. S. Markosyan, B. V. Mill, S. Y. Reiman, V. V. Snegirev, and S. A. Tamazyan, Sov. Phys. Solid State **31**, 233 (1989).

[6] Powder Diffraction File, card No. 38–288, International Centre for Diffraction Data, Newtown Square, PA.

[7] P. E. Werner, TREOR trial and error program for indexing of unknown powder patterns, Department of Structural Chemistry, Arrhenius Laboratory, University of Stockholm, Sweden (unpublished).

[8] J. Rodríguez Carvajal, FULLPROF program for Rietveld refinement and pattern matching analysis (unpublished). The program is a strongly modified version of that described by D. B. Wiles and R. A. Young, J. Appl. Crystallogr. **14**, 149 (1981).

[9] A. Altomare, G. Cascarano, C. Giacovazzo, A. Guagliardi, M. C. Burla, G. Polidori, and M. Cammalli, SIRPOW.91 (semi-invariants representation applied to powder data), J. Appl. Crystallogr. **27**, 435 (1994).

[10] P. J. Brown, Report No. SP88BR5016, Institute Loue-Langevin, Grenable, France (unpublished).

[11] E. A. Boudreaux and L. N. Mulay, *Theory and Applications of Molecular Paramagnetism* (Wiley, New York, 1976), pp. 494–495.

[12] See AIP Document No. PAPS PRBMDO-57-5240 for 5 pages of tables containing observed d spacings and intensities of each hkl peak for both R=Y and Tb compounds. Order by PAPS number and journal reference from American Institute of Physics, Physics, Physics Auxiliary Publication Service, Carolyn Gehlbach, 500 Sunnyside Boulevard, Woodbury, NY 11797-2999. Fax: 516-576-2223, e-mail: paps@aip.org. The price is $1.50 for each microfiche (98 pages) or $5.00 for photocopies of up to 30 pages, and $0.15 for each additional page over 30 pages. Airmail additional. Make checks payable to the American Institute of Physics. These tables can also be obtained from the authors.

[13] M. Nardelli, PARST system of computer routines for calculating molecular parameters from results of crystal structure analysis, University of Parma, Italy, 1982 (unpublished).

[14] J. A. Campá, E. Gutiérrez Puebla, M. A. Monge, C. Ruíz Valero, J. Mira, J. Rivas, C. Cascales, and I. Rasines, J. Solid State Chem. **120**, 254 (1995).

[15] J. A. Campá, C. Cascales, E. Gutiérrez Puebla, M. A. Monge, I. Rasines, and C. Ruíz Valero, J. Solid State Chem. **124**, 17 (1996).

[16] G. E. Bacon, *Neutron Diffraction* (Oxford University Press, New York, 1975).

[17] E. F. Bertaut, Acta Crystallogr., Sect. A: Found. Crystallogr. **24**, 217 (1968).

[18] E. García Matres, J. L. García Muñoz, J. L. Martínez, and J.Ro-

driguéz Carvajal, J. Magn. Magn. Mater. **149**, 363 (1995).

[19] G. G. Chepurko, Z. A. Kazei, D. A. Dudrjavtsev, R. Z. Levitin, B. V. Mill, M. N. Popova, and V. V. Snegirev, Phys. Lett. A **157**, 81 (1991).

[20] M. N. Popova, in Proceedings of the 3rd International Conference on f Elements, Paris, 1997 [J. Alloys Compounds (to be published)].

[21] J. Amador, E. Gutiérrez Puebla, M. A. Monge, I. Rasines, C. Ruíz Valero, F. Fernández, R. Sáez Puche, and J. Campá, Phys. Rev. B **42**, 7918 (1990).